forests

Article

Determination of Riparian Vegetation Biomass from an Unmanned Aerial Vehicle (UAV)

Alessandro Matese [1], Andrea Berton [2], Valentina Chiarello [3], Riccardo Dainelli [1], Carla Nati [1], Laura Pastonchi [1], Piero Toscano [1,*] and Salvatore Filippo Di Gennaro [1]

[1] Institute of BioEconomy, National Research Council (CNR-IBE), Via G. Caproni 8, 50145 Florence, Italy; alessandro.matese@cnr.it (A.M.); riccardo.dainelli@cnr.ibe.it (R.D.); carla.nati@cnr.ibe.it (C.N.); laura.pastonchi@cnr.ibe.it (L.P.); salvatorefilippo.digennaro@cnr.it (S.F.D.G.)
[2] Institute of Clinical Physiology (IFC), National Research Council (CNR), Via Moruzzi 1, 56124 Pisa, Italy; andrea.berton@cnr.it
[3] Consorzio di Bonifica 6 Toscana Sud (CB6), Via Leonardo Ximenes 3, 58100 Grosseto, Italy; v.chiarello@cb6toscanasud.it
* Correspondence: piero.toscano@ibe.cnr.it; Tel.: +39-05-5303-3747

Abstract: The need to rely on accurate information about the wood biomass available in riparian zones under management, inspired the land reclamation authority of southern Tuscany to develop a research based on the new remote sensing technologies. With this aim, a series of unmanned aerial vehicle (UAV) flight campaigns flanked by ground-data collection were carried out on 5 zones and 15 stream reaches belonging to 3 rivers and 7 creeks, being representative of the whole area under treatment, characterized by a heterogeneous spatial distribution of trees and shrubs of different sizes and ages, whose species' mix is typical of this climatic belt. A careful preliminary analysis of the zones under investigation, based on the available local orthophotos, followed by a quick pilot inspection of the riverbank segments selected for trials, was crucial for choosing the test sites. The analysis of a dataset composed of both measured and remotely sensed acquired parameters allowed a system of four allometric models to be built for estimating the trees' biomass. All four developed models showed good results, with the highest correlation found in the fourth model (Model 4, R^2 = 0.63), which also presented the lowest RMSE (0.09 Mg). The biomass values calculated with Model 4 were in line with those provided by the land reclamation authority for selective thinning, ranging from 38.9 to 70.9 Mg ha^{-1}. Conversely, Model 2 widely overestimated the actual data, while Model 1 and Model 3 offered intermediate results. The proposed methodology based on these new technologies enabled an accurate estimation of the wood biomass in a riverbank environment, overcoming the limits of a traditional ground monitoring and improving management strategies to benefit the river system and its ecosystems.

Keywords: precision forestry; unmanned aerial vehicle; image analysis; crown detection; biomass; river analysis

Citation: Matese, A.; Berton, A.; Chiarello, V.; Dainelli, R.; Nati, C.; Pastonchi, L.; Toscano, P.; Di Gennaro, S.F. Determination of Riparian Vegetation Biomass from an Unmanned Aerial Vehicle (UAV). *Forests* **2021**, *12*, 1566. https://doi.org/10.3390/f12111566

Academic Editor: Krzysztof Stereńczak

Received: 19 October 2021
Accepted: 10 November 2021
Published: 12 November 2021

1. Introduction

Riparian zones are dynamic and complex ecosystems because they are shaped by fluvial geomorphic processes that involve different components including stream channels, banks, vegetative cover, and floodplains [1,2]. Among these, riparian vegetation located on waterways has a central position in the river ecosystem. It stands at the interface of terrestrial and aquatic environments and therefore plays a crucial role both for the ecological integrity of river courses and for hydrogeological processes [3–5]. Living and dead plants have a physical impact on water runoff through complex hydraulic interactions during baseflows as well as overbank flows, besides their impact on water quality and water uptake, storage, and return to the atmosphere [6–9]. The fact that in Europe about 90% of riparian zones have disappeared or are degraded shows how much these areas need to be monitored more [10]. Unfortunately, some processes localized along the riverbanks are unpredictable, e.g., the encroachment of invasive riparian species with great reductions of the spatial extent of water flow [5], and can fluctuate dramatically over time. As a result, the natural complexity of a riverscape is difficult to quantify [2]. Furthermore, the instability of these areas is not only due to natural factors, but, in the last decades, human pressures have severely affected the equilibrium of these zones, making efforts to understand riparian ecosystems more difficult [5,11]. As a consequence of this scenario, river ecosystems are currently under the attention of the European legislature, which encourages their safeguarding through adequate monitoring and management activities [10,12]. Both researchers and local stakeholders need effective tools to monitor riparian vegetation: the former for a detailed understanding of riparian ecosystems dynamics and the latter for a quantitative evaluation of the costs and benefits of the actions to be taken [3]. Within this framework, accurate information about riparian ecosystems, such as land cover, above-ground biomass (AGB) and leaf area index (LAI), canopy closure, and vertical canopy structure, are important parameters for good conservation and management plans [13,14]. Although the traditional ground approach based on in situ optical and radar measurements has given good results for many ecological applications, it presents several limitations [15,16]. First of all, field surveys are labor-intensive, time-consuming, expensive, and sometimes risky for operators. They cannot be applied to large areas, consequently drastically limiting the amount of data that can be collected [17], especially in hard to access forested zones. They also cannot fully represent a three-dimensional spatial pattern of vegetation because they produce only two-dimensional (x and y) images. Furthermore, their sensitivity and accuracy decrease with AGB and LAI [3,18]. All these limits are nowadays overcome by the recent developments in remote sensing (RS) platforms and geographic information systems (GISs), which have proven to be efficient tools to analyze the vegetation cover in different sectors [3,10,14,19–31]. RS platforms, such as satellite systems, aircrafts, and unmanned aerial vehicles (UAVs), have different peculiarities exploited for different issues under investigation. Satellite solutions are a fundamental tool for long-term and extensive monitoring in forestry activities [32]. Airborne platforms, instead, provide a higher level of detail compared to satellites but require a higher effort in flight planning [12,29,33]. Unfortunately, the cost and/or the low resolution of imagery provided by these platforms often discourage their use for the detection of some vegetation parameters, such as biomass estimation [14]. The UAV represents a fast, flexible, and low-cost tool that can easily provide images of the investigated areas with a very high spatial resolution. UAVs can fly on pre-programmed routes, and they allow investigation of the forest structure by flying at a low altitude for several hectares, thus acquiring images in optimal weather conditions (low wind and clear sky conditions) [31,34]. These RS technologies represent a fundamental tool for precision forestry (PF). The PF concept concerns planning, monitoring, and conducting site-specific forest management activities and operations to improve wood product quality and utilization, reduce waste, increase profits, and maintain the quality of the environment [35]. Multitemporal analysis and timeliness are key requirements to enable the adoption of PF practices [29]. This is especially true when the forest structure is changing rapidly [36], as in managed riparian buffer zones. According to the latest findings in PF applications, UAVs have been equipped with a wide range of optical sensors [37–41] and employed mostly for forest health monitoring and diseases mapping [37,42–44], recovery monitoring after fire events or conservation interventions [39,45,46], tree species classification and invasive plants detection [33,47–52], and, as a top research topic, estimation of dendrometric parameters, such as the dominant height, stem number, crown area, volume, and AGB [14,28,29,53–62]. It is possible to estimate tree biomass directly from two tree architectural properties that can be remotely measured: tree height (H) and crown diameter (CD) [53]. A methodological approach to estimate these parameters is to use the RGB images and structure from motion (SfM) algorithms to provide a high 3D geometric reconstruction of the investigated area [14]. To analyze these data, tree height models, such as the canopy height model (CHM), are used [28]. The application of an unsupervised algorithm to realize individual tree crown segmentation is a high-performance methodology to localize individual trees from raster images and thus estimate their crowns, heights, and positions [29]. This step is complex, particularly in broadleaf, mixed, or multi-layered forests and, therefore, also in riparian areas, where similar conditions can be found. This difficulty is generally due to an inability to determine the appropriate kernel size to simultaneously minimize omission and commission error concerning tree stem identification [63]. For the aforementioned difficulties, the adoption of PF in riparian zones is currently limited to a few studies [3,64–73]. Moreover, to the authors' knowledge, none of these studies have dealt with UAV estimation of riparian vegetation biomass in the Mediterranean area except for the one conducted by [72], who estimated carbon stocks for ecological purposes. It is from the need to fill this current information gap that the present study was conceived, also because the estimation of biomass potentially available through riparian maintenance works can provide an economic return for local stakeholders. The purpose of this study was to identify a rapid and easily reproducible technique for wood biomass estimation in riparian zones through imagery acquisition from a UAV platform. Pursuing this aim, a flight campaign flanked by a ground data collection was carried out in the south of Tuscany (Italy). The area is characterized by a complex physical geography, extreme morphological heterogeneity, and a temperate climate, typical of the Mediterranean Basin. About 60% of lands in Tuscany suffer from flood and flash flood events [11], thus the vegetation constantly changes over time as a consequence of this natural disturbance [74]. For this reason, monitoring and management is necessary to restore the waterways' hydraulic efficiency. In this area, a thinning intervention on the vegetation along the riverbanks was scheduled for management tasks. The methodology implemented in the study will help to enable the control of large areas of interest that need regular maintenance, thus overcoming the limits of a traditional approach based only on ground observations. Moreover, this procedure underpinned by RGB interpretation and the 3D model obtained from UAV and the allometric determination derived from the simplified modeling approach allows its application both in different environments and at different spatial scales.

2. Materials and Methods

2.1. Study Area

The study took place between June and July 2019, upon a request received from the land reclamation consortium Consorzio di Bonifica 6 Toscana Sud (CB6), a public authority active in the southern part of Tuscany for water management, land conservation, and environment protection. CB6 had planned a thinning activity in the Provinces of Siena and Grosseto and was interested in a fast and accurate assessment of the wood biomass available for economic reasons and for energy demand. As a first step, a preliminary survey was conducted by analyzing the orthophotos available in the regional database, focusing on sites' main morpho-vegetational characteristics. In the hydrographic district under investigation, amounting to about 120 hectares (ha), 5 zones (see Figure 1) and 15 stream reaches belonging to 3 rivers and 7 creeks (see Table 1) were selected as being representative of the whole area and characterized by a heterogeneous spatial distribution of trees and shrubs of different sizes and ages, whose species' mix was typical of this climatic belt.

2.2. Test Sites and Ground-Data Collection (GDC)

Within the transects under investigation (A–F, Table 1), dendrometric measurements of the standing trees were taken at ground level (GDC) to develop appropriate allometric models for quantifying the available biomass. In some cases, it was chosen to monitor both sides of the riverbeds while in others only a single part. Survey conditions were particularly difficult due to the presence of dense herbaceous-shrub vegetation with a prevalence of bramble (*Rubus* spp.). As an example, a zoom of the tested area located along the Bruna River (Site STR-5) is shown below (Figure 2).

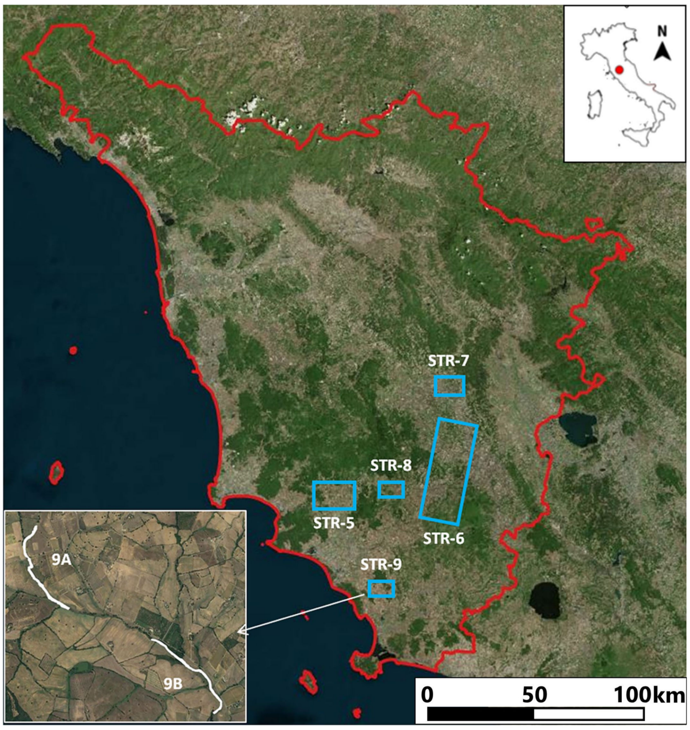

Figure 1. The study zones (highlighted in blue) selected within the Regione Toscana area (highlighted in red) and a zoom of two Osa River reaches where detailed information was acquired (highlighted in white).

Table 1. Study area and experimental campaign description (* UAV's flight ID, ** Ground-data collection ID).

Zone ID	Location	Waterway Segment	Type	ID_UAV *	GDC ID **
STR-5	42°53′18.22″ N 11°33′41.57″ E	Bruna 5A	River	5A	A
		Bruna 5B	River	5B	B
		Asina	Creek	5C	
		Rigo	Creek	5D	C
STR-6	42°53′18.22″ N 11°33′41.57″ E	Asso	Creek	6A	
		Orcia	River	6B	
		Tuoma	Creek	6C	
		Ente	Creek	6D	
STR-7	42°53′18.22″ N 11°33′41.57″ E	Ombrone 7A	River	7A	D
		Ombrone 7B	River	7B	
STR-8	42°53′18.22″ N 11°33′41.57″ E	Ombrone 8A	River	8A	E
		Ombrone 8B	River	8B	
		Gretano	Creek	8C	F
STR-9	42°53′18.22″ N 11°33′41.57″ E	Osa 9A	Creek	9A	
		Osa 9B	Creek	9B	

The length of transects was measured with a metric tape and the border points were georeferenced with a differential GPS (Leica GS09 GNSS, Leica Geosystems AG, accuracy of 0.02 m). The vegetation of each segment was surveyed by ground observations, recording the number of trees, GPS position, species, diameter at breast height (DBH), height (H), and vegetative status. DBHs were measured with a dendrometric caliper while Hs were recorded with a hypsometer (Nikon Forestry Pro). Once H and DBH had been recorded for each tree, a "double-entry-tables" system provided by the Italian National Forest Inventory [75] was used to estimate the corresponding dendrometric volume (m^3). These tables provide the dendrometric volume (i.e., tree's volume excluding branches) for the majority of Italian tree species distinguished by phytoclimatic belts. However, some poplars measured in the transects exceeded the range of H and/or DBH, and some minor species were not reported. In both cases, dedicated allometric equations [75] were applied, respectively:

$$v = 5.42876 \cdot 10^{-5} \cdot d^{1.7885} \cdot h^{1.0286} \quad (1)$$

for poplar (1), where v = volume (m^3), d = DBH (cm) and h = H (m):

$$v = -1.614 \cdot 10^{-3} + 3.72428 \cdot 10^{-5} \cdot d^2 \cdot h + 9.59885 \cdot 10^{-4} \cdot d - 2.40608 \cdot 10^{-4} \cdot h \quad (2)$$

for other broadleaf species (2). To convert volume into mass units (Mg), the former was multiplied by the specific tree species' mass density [76].

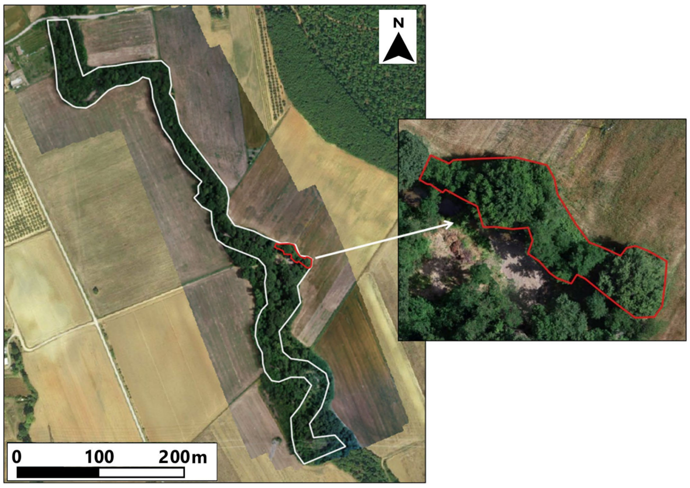

Figure 2. Study site (red polygon) localized along ID_UAV 5B (white polygon) of Bruna River.

2.3. UAV Data Collection and Processing

Over the selected transects, a UAV flight campaign was designed, to cover the whole stand's variability. As a preliminary step, a fine-tuning calibration of the UAV system was performed, comparing field ground measurements and remotely sensed data. A DJI Phantom 4 Pro UAV platform was deployed in the study campaign (Figure 3), a model designed with a magnesium alloy structure, robust and capable of absorbing vibrations, and characterized by a higher center of gravity that provides great balance and flight agility at the same time.

Figure 3. DJI Phantom 4 Pro used during UAV flight campaigns.

The UAV used can fly for up to 28 min, within a range of 5 km and is equipped with an HD video transmission. The integrated 3-axis gimbal allows camera stabilization for taking high-resolution photos at 20 megapixels. During the planning phase, different flight altitudes were tested to guarantee a good compromise between the spatial resolution of the acquired RGB images and the survey speed. The flight altitude identified to ensure an optimal characterization of vegetation in the monitored areas was 90 m, providing

0.025 m per pixel ground resolution. Furthermore, recording in clear sky conditions was fundamental to obtain good results. Three-dimensional photogrammetric reconstruction also requires a high image overlap, which was achieved by setting a low forward speed (frontal overlap) and narrow flight transepts (lateral overlap). In this study, the overlap percentage set among frames was 80%. This type of flight, being characterized by the acquisition of small surfaces per unit of time, allowed the maximum accuracy of geometric reconstruction of the vegetation to be achieved, and therefore precision in estimating biomass. This data processing workflow was also adopted in a recent work by the authors to estimate the pruning biomass recovered from uneven-aged and irregularly spaced chestnut orchards in central Italy through the use of multispectral data [29]. The RGB images' processing requires a high computing power; for this reason, it was operated by a workstation equipped with 2 Intel Xeon E7 v.4 processors, an NVIDIA Quadro M6000 video card with 24 dedicated GB, and an RAM with 256 GB. Figure 4 reports the different software involved in the image processing workflow.

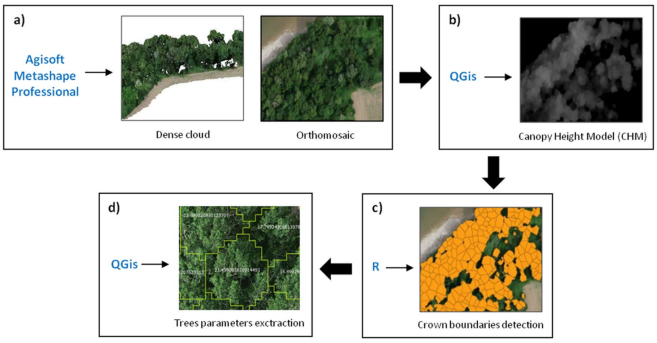

Figure 4. Processing chain of UAV data acquired: dense cloud and orthomosaic (**a**), canopy height model CHM (**b**), trees' position and crown boundaries (**c**), and main tree parameters (**d**).

During the first phase, the Agisoft Metashape Professional software, Edition 1.5.2 (https://www.agisoft.com, accessed on 14 September 2021) was used. This Structure from Motion (SfM) processing software, through a special processing chain that exploits the high overlap level of the RGB images acquired by UAV, generates the dense point cloud (3D model) and the orthomosaic of each investigated site of interest (Figure 4a). The dense cloud was imported into QGis software (https://www.qgis.org/it/site/, accessed on 11 July 2021) to develop, through LAStools toolbox (https://laszip.org/, accessed on 6 June 2021), the CHM, a raster file of trees located in the sites (Figure 4b). The LAStools pipeline called "flightlines to single CHM (pit-free)" was used to convert LAS files, 3D point cloud exported by Agisoft Metashape, into a single pit-free CHM using the algorithms described by [77]. The CHM accuracy was analyzed comparing the vegetation height measurements collected during the field campaigns and the resolution chosen for this model at 0.5 m. This stage is usually exploited to detect the tree top, visualize the crown shape, or estimate the tree volume [28]. The next image processing step concerned the use of 'rLIDAR' script (version 0.1.1) [78] in the R programming language (version 3.6.0). In this study, it enabled the unsupervised generation of a vector file relative to the position and crown boundaries of trees within the CHM (Figure 4c). First of all, CHM smoothing, based on local maxima, was applied to remove noise and to improve over-segmentation errors. The tops of individual trees were then automatically detected using the CHM and the local maximum search method (rLiDAR: FindTreesCHM function) with a Fixed Window Size (FWS) of 3 $\times$ 3 pixels resulting as the best window. The threshold for the lowest tree height (Minht value) was fixed at 3.0 m to avoid the misdetection of undergrowth. The ForestCAS function (cf. rLiDAR), based on a centroidal Voronoi tessellation approach, was then applied to automatically isolate each tree crown polygon [78,79]. The threshold for the Maximum Crown Radius (Maxcrown) was set at 10.0 m, according to the dendrometric characteristics of the sites. After isolating each tree boundary and clipping them from the

CHM, the grid cells with values below 50% of the maximum height measured for each tree were excluded (Exclusion values) to eliminate the low-lying noise. Finally, the vector file including each tree boundary characteristic was analyzed in a GIS environment to extract the tree parameters necessary for spatial estimation of biomass (Figure 4d): H and CD.

2.4. Biomass Estimation Methodology

As highlighted before, tree biomass can be estimated by two dendrometric parameters: H and CD. H was measured for each tree placed in the studied segments (Section 2.2), whereas CD was extracted through an on-screen interpretation of two products: orthomosaic and CHM (Figure 5). This choice was made because, in sites where there is dense vegetation, such as those investigated in this study, the remotely sensed identification of CD allows the processing times to be shortened, thanks also to the high resolution of the two aforementioned products. The manually drawn individual crown polygons approach has already been exploited in association with the unsupervised approach by the scientific community for the detection of trees' parameters [29,80].

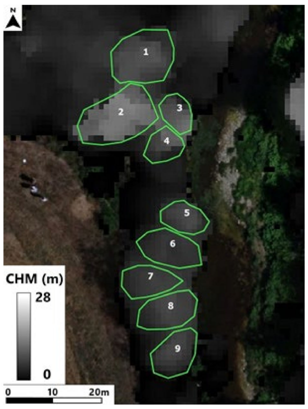

Figure 5. Orthomosaic and canopy height model (CHM) (with transparency for values = 0) used for on-screen interpretation to extract trees' CD.

Using this database (composed of both measured and remotely sensed parameters) and estimated biomass for each tree as indicated in Section 2.2, allometric models with a power relationship were developed to detect the biomass of the whole monitored areas. LAB Fit Curve Fitting Software v. 7.2.50 [81] was used to build the following Models (3–6):

$$Y = A \cdot X^{B} \quad \text{(Model 1 3)}$$

$$Y = A \cdot X^{(B \cdot X)} \quad \text{(Model 2 4)}$$

$$Y = A \cdot (X_1 \cdot X_2)^{B} \quad \text{(Model 3 5)}$$

$$Y = A \cdot X_1^{(B \cdot X_2)} \quad \text{(Model 4 6)}$$

The first two models relate H (X-independent variable) to biomass (Y-dependent variable), whereas in Model 3 and Model 4, biomass (Y) is estimated through two independent variables related, respectively, to CD (X_1) and H (X_2). A and B are multiplicative parameters in all four models. The coefficient of determination (R^2) and root mean square error (RMSE) were computed for the aforementioned regressions.

2.5. Model Validation

Selected trees located both in the bed and on the bank of the rivers were removed according to the thinning plan. The logging company's team was composed of 4 operators, 2 equipped with chainsaws, one with an excavator for severing and piling logs, and the last one with a forwarder for the extraction. Wood was stored to dry in several piles, waiting to be chipped at a later date. CB6 carried out felling in 4 out of the 5 surveyed zones (STR-5, STR-7, STR-8, STR-9), on a larger area compared to the one covered by UAV flights.

Therefore, to compare remotely sensed biomass with the measured one, the estimated amount of biomass per unit of surface (Mg ha^{-1}) was multiplied by the total area affected by cuts. Through this comparison, it was possible to determine whether our regression models could be used to generate an accurate biomass estimation. This can be defined as an indirect check of its reliability when applied to large areas. The methodology used deals with a training and validation dataset but does not follow a standardized approach. Indeed, the training dataset encompasses all trees measured during the ground data collection in the test site (180 trees, Table 2), while the validation was performed against all the trees in the area covered by UAV flights (total number of the trees > 1000). Considering that the Consorzio di Bonifica provided a total amount of pruned biomass, our validation refers to this value (cumulated total biomass removed).

Table 2. Main features of the test sites and ground-collected allometric data.

GDC Site	Length	Surface	Trees	Species		DBH	H	CD	Biomass
	m	m^2	N	Type	%	cm	m	m	Mg
A	108	1135	25	*Populus nigra* *Robinia pseudoacacia* *Acer monspessulanum* *Quercus ilex*	45 19 18 18	26.83 ± 16.30	11.40 ± 3.96	7.65 ± 3.36	0.18 ± 0.27
B	68	884	15	*Quercus pubescens* *Robinia pseudoacacia* *Populus nigra*	50 44 6	23.67 ± 6.53	13.55 ± 2.34	5.23 ± 0.42	0.25 ± 0.16
C	34	568	15	*Populus nigra* *Quercus ilex*	87 13	24.25 ± 13.26	10.52 ± 2.26	3.92 ± 1.43	0.12 ± 0.15
D	190	2296	80	*Robinia pseudoacacia* *Populus nigra* *Salix alba*	80 15 5	16.55 ± 8.41	10.82 ± 2.83	4.94 ± 1.14	0.13 ± 0.13
E	25	479	26	*Populus nigra* *Salix alba*	70 30	28.88 ± 8.03	13.60 ± 3.75	3.97 ± 0.77	0.18 ± 0.12
F	43	554	19	*Populus nigra* *Robinia pseudoacacia* *Salix alba* *Ulmus minor* *Alnus glutinosa*	59 23 9 5 4	19.64 ± 5.82	13.40 ± 4.56	5.83 ± 2.72	0.26 ± 0.15

3. Results

3.1. Ground Data Collection (GDC)

Table 2 shows the main features of each tested segment (length, surface, number of trees, species) and the ground-collected allometric data, such as DBH, H, and CD, collected with ground-based measured biomass. For each allometric characteristic, mean values and standard deviations are reported. Most of the surveyed species were typical of riparian vegetation, such as black poplar (*Populus nigra*), black locust (*Robinia pseudoacacia*), white willow (*Salix alba*), field elm (*Ulmus minor*), and common alder (*Alnus glutinosa*). However, there was a small group of thermophilic species strictly belonging to Mediterranean scrub, such as downy oak (*Quercus pubescens*), holm oak (*Quercus ilex*), and Montpellier maple (*Acer monspessulanum*). Overall, the most pervasive species across the six test areas were poplar and black locust, the latter an alien plant that exploits its vegetative reproduction to spread widely in wetlands. A description of the experimental results is given, their interpretation, as well as the conclusions that can be drawn.

The GDC A site (located in the Bruna 5A segment) was adjacent to a tomato field and had a narrow and long rectangular shape (10.5 m × 108 m). Many patches contained invasive plants, such as giant reed (*Arundo donax*) and black locust, grouped in 8–10 specimens (small trees not recorded) (Figure 6a). Although the surveyed area was large (1135 m^2), it had a low tree density (on average DBH > 10 cm and H = 1.40 m). Nevertheless, the highest CDs were detected here (7.65 m), owing to some large and mature trees. This heterogeneity was also reflected in the variability of the estimated biomass (±0.27 Mg). GDC B (located in the Bruna 5B segment) was enclosed between cultivated fields and characterized by a high number of downy oak and black locust (Figure 6b), while only a few black poplar trees were present. Concerning shrub vegetation, common hawthorn (*Crataegus monogyna*) was widely spread in the understory and this made the survey area particularly difficult to access. Hs were on average greater than 13 m with slight variability, while DBHs reached an average value close to 24 cm. Numerous plants were lying on the ground or in the watercourse bed and, amid high vegetation, many smaller trees did not have the minimum size needed to be recorded (DBH < 3 cm), thus affecting the tree density. Biomass registered here had the highest values among the six test areas and this is consistent with the medium-high values for all the other allometric quantities taken into consideration (DBH, H, CD; see Table 2).

Figure 6. Vegetation pattern and distribution within the six test segments (capital letters correspond to the test area ID, Table 2).

GDC C (Rigo creek, Figure 6c) was located on the left bank next to an abandoned field with scattered olive trees. The few trees (15) were all black poplars except for two holm oaks. They had the lowest heights (10.52 m) among the six test areas with reduced variability. Regarding the crown diameters, the lowest average values were found (3.92 m) and this affected the low average biomass (0.12 Mg).

GDC D (Ombrone 6A) and GDC E (Ombrone 8A) were the only study sites located on the main watercourse (river Ombrone) of the study hydrographic network. In GDC D, the most widespread species was the allochthonous and invasive black locust (Figure 6d). Other species, like black poplar and white willow, were sporadic with isolated large trees, especially of the former. It was characterized by an elongated rectangular shape with a very steep scarp at the beginning and end of the stretch and with a double-terraced riverbank profile in the central section. The dense vegetation alternated with sections in which trees were absent; nevertheless, the number of trees detected was the highest of all the test areas (80), also due to the biggest surface (2296 m^2). The surveyed trees had very low values regarding both H (10.82 m) and DBH (16.55 m). In particular, the presence of small trees was also worthy of note (28 specimens) with DBH < 10 cm (Figure 6d), which, however, can contribute significantly to the total biomass. GDC E was characterized by a rectangular shape, and it was placed in the closest zone to the river floodplain, in the lower course of the river. Although Ombrone 8A is the smallest test area among those considered (479 m^2), it had the highest trees density (5.4 trees/100 m^{-2}) (Figure 6e). This was composed mainly of black poplar and to a lesser extent of white willow, with the highest average values in terms of DBH (28.88 cm) and H (13.60 m) among all the surveyed areas. GDC F (Gretano creek) consisted of two separate but close blocks. The first block included a few large trees while the second was composed of dense and multi-layer vegetation of mixed species, with an understory rich in young trees (Figure 6f). The spatial separation between the two blocks contributes to the vegetation unevenness, which is reflected in the highest variability among all the test areas in terms of the detected species (five, Table 2). Moreover, the test area presented the lowest amount of biomass (0.09 Mg) with a small standard deviation due to the presence of many young trees of a similar size.

3.2. UAV Estimated Dataset

Table 3 shows the remotely sensed dataset acquired through UAV campaigns for the five studied zones.

Table 3. UAV remotely sensed dataset acquired for the five monitored sites.

Zone ID	ID_UAV (GDC Site)	Total Area (ha)	Σ Crown Areas (ha)	Tree Cover (%)	H (m)	CD (m)
STR-5	5A (A)	3.14	2.09	67	14.33 ± 5.57	4.88 ± 1.56
	5B (B)	4.16	2.69	64	12.96 ± 4.53	5.19 ± 1.74
	5C	3.67	2.22	60	16.56 ± 6.87	5.06 ± 1.60
	5D (C)	8.27	3.43	42	10.71 ± 3.76	5.10 ± 1.49
STR-6	6A	1.30	1.07	82	19.87 ± 4.58	5.79 ± 1.49
	6B	2.97	2.61	88	14.62 ± 5.25	5.07 ± 1.36
	6C	1.08	0.88	81	16.66 ± 4.15	5.65 ± 1.25
	6D	1.97	1.62	82	18.40 ± 6.51	5.98 ± 1.35
STR-7	7A (D)	1.10	0.92	84	11.20 ± 5.55	4.56 ± 1.19
	7B	1.58	1.42	90	12.37 ± 5.71	5.12 ± 1.43
STR-8	8A (E)	6.43	3.03	47	13.74 ± 5.47	5.18 ± 1.60
	8B	4.34	0.94	22	15.96 ± 7.20	3.72 ± 1.70
	8C (F)	1.15	0.65	57	18.83 ± 6.32	4.79 ± 1.98
STR-9	9A	1.35	1.25	92	13.43 ± 4.52	5.57 ± 1.50
	9B	1.56	1.18	75	12.97 ± 6.05	5.52 ± 1.53

In Figure 7, zones flown over by the UAV are drawn as white polygons, while trees' crown segmentation areas are reported in green. Using these parameters, the percentage of tree cover was identified. Lastly, the average H and CD values of trees present in every cutting area were estimated. Trees that had an H value lower than 3 m were not taken into consideration because this range was not affected by the cuts made by CB6. The highest variability among the data shown in Table 3 occurred in the tree cover percentage values. They ranged from 22% in site 8B (Ombrone) to 92% in site 9A (Osa) (see Figure 7). Moving on to the tree's dendrometric parameters, always within the two aforementioned areas, the highest and lowest CD value was found. It can be observed that site 8B had an average CD of 3.72 m, whereas in site 6D, the highest CD was equal to 5.98 m. Regarding the average tree height, this ranged from 10.71 (site 5D, Rigo) to 19.87 m (site 6A, Asso), and the highest variability of this parameter was detected in site 8B (± 7.20 m). The lowest heights recorded along the 5D (Rigo) were also highlighted among the six test areas during the GDC (Table 2).

3.3. Regression Models

Through the UAV remote sensing activity, it was possible to estimate the woody biomass within the monitored stream reaches. As mentioned in Section 2.4, the dendrometric parameters H and CD represent an effective approach for trees' biomass estimation. The relations (equations and R^2) connecting these two variables and the estimated biomass within the five studied zones are presented in Table 4. Particularly, the first two models link only measured height (X-independent variable) to the estimated biomass (Y-dependent variable), whereas in the last two models, the biomass (Y) is estimated through two independent variables: manually contoured CD (X_1) and ground-measured H (X_2).

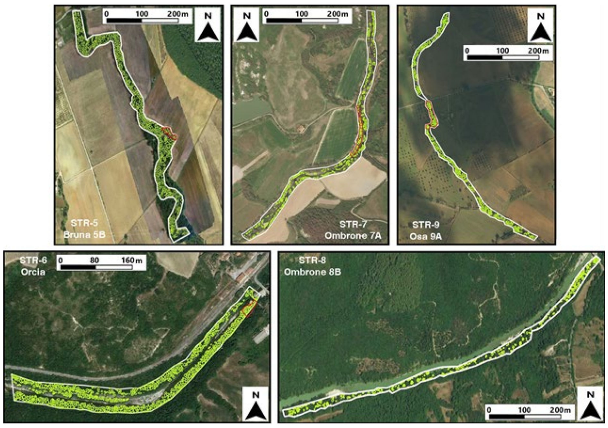

Figure 7. Tree crown segmentation areas (colored in green) identified within cutting polygons (in white) indicated by the CB6. Red area represents GDC study sites.

Table 4. Equations and R^2 of the four adopted regression models.

N°	Equation	R^2	RMSE (Mg)
Model 1	$Y = 0.0001 \cdot X^{2.8377}$	0.56	0.10
Model 2	$Y = 0.0221 \cdot X^{(0.5687 \cdot X)}$	0.57	0.10
Model 3	$Y = 0.0020 \cdot (X_1 \cdot X_2)^{1.0737}$	0.59	0.18
Model 4	$Y = 0.0502 \cdot X_1{}^{(0.0576 \cdot X_2)}$	0.63	0.09

All four developed models show interesting results, with the highest correlation found in the fourth (Model 4, R^2 = 0.63), which also presents the lowest RMSE equal to 0.09 Mg.

3.4. Biomass Estimation

Table 5 shows the estimated biomass results (tree average biomass and biomass per unit of surface) obtained through the four aforementioned models (Table 4) within each parcel. Regarding tree average biomass (Mg), it can be observed that through Model 2, the highest values with the highest variability were obtained, and the maximum value reaches 1.22 Mg in the 6D (STR-6) and 8C (STR-8 sites). This relation probably tends to overestimate the values. The other three power relationships, instead, provide averagely comparable values; in fact, they range from 0.14 Mg in the 7A (STR-7) to 0.60 Mg estimated in the 6A site (STR-6).

The total tree biomass divided by the area of each segment allowed the available amount of biomass per hectare (Mg ha^{-1}) to be calculated. A wide variability was observed within these results. The second model overestimated the biomass results for all sites, whereas the lowest value was found in the 5D segment (23.0 Mg ha^{-1}) by applying the first model.

3.5. Comparison between Estimated and Measured Dataset

At the end of October 2019, thinning was carried out in zones STR-5, STR-8, and STR-9 by the forestry companies in the manner indicated in Section 2.5. Thinned surface (ha), selective cutting grade (%) adopted in each zone, measured biomass (Mg), and average UAV estimated biomass of each zone (Mg ha^{-1}) using the four models (see Table 4) are shown in Table 6. Regarding the UAV total biomass (Mg), this was calculated by averaging the biomass per unit of surface (Mg ha^{-1}) covered by flights within the three thinned zones (see Table 5), and multiplying it by the respective surface, taking into account the cutting percentage applied.

The results showed that Model 4 exhibits the highest accuracy with a tendency to underestimate cut biomass and the lowest absolute errors, represented by 67 Mg for STR-5, 66 Mg for STR-8, and 10 Mg for STR-9, while Model 1 performs better for STR-7 with a slight overestimation of 26 Mg. Conversely, Model 2 widely overestimates the actual data and Model 3 offers intermediate results. Thinning was not done in the 8C site of STR-8, thus the average UAV estimated biomass for STR-8 was calculated by averaging the values from 8A and 8B.

Table 5. Tree average biomass (Mg) and biomass per surface (Mg ha^{-1}) estimated for each UAV flight through the four models previously shown in Table 4.

Zone ID	ID_UAV	Total Area (ha)	Biomass Per Tree (Mg)				Biomass (Mg ha^{-1})			
			Model 1	Model 2	Model 3	Model 4	Model 1	Model 2	Model 3	Model 4
STR-5	5A	3.14	0.30 ± 0.03	0.47 ± 0.09	0.20 ± 0.01	0.23 ± 0.02	96.0	151.5	63.3	74.0
	5B	4.16	0.21 ± 0.02	0.25 ± 0.04	0.19 ± 0.01	0.20 ± 0.01	57.7	68.1	52.0	55.0
	5C	3.67	0.47 ± 0.05	1.03 ± 0.16	0.23 ± 0.01	0.30 ± 0.03	127.1	281.9	63.8	82.7
	5D	8.27	0.12 ± 0.01	0.13 ± 0.01	0.15 ± 0.01	0.15 ± 0.01	23.0	24.7	27.8	27.9
STR-6	6A	1.30	0.60 ± 0.03	1.06 ± 0.11	0.24 ± 0.01	0.31 ± 0.02	271.8	475.5	109.9	140.1
	6B	2.97	0.30 ± 0.02	0.38 ± 0.05	0.20 ± 0.01	0.23 ± 0.01	120.2	153.0	83.4	92.4
	6C	1.08	0.37 ± 0.02	0.47 ± 0.04	0.20 ± 0.01	0.22 ± 0.01	180.1	226.3	94.9	107.3
	6D	1.97	0.57 ± 0.05	1.22 ± 0.16	0.24 ± 0.02	0.32 ± 0.03	196.8	425.0	84.4	110.7
STR-7	7A	1.10	0.18 ± 0.03	0.28 ± 0.07	0.14 ± 0.01	0.16 ± 0.01	86.4	133.9	65.6	75.3
	7B	1.58	0.22 ± 0.03	0.33 ± 0.08	0.18 ± 0.01	0.20 ± 0.02	89.1	134.3	71.5	80.6
STR-8	8A	6.43	0.29 ± 0.03	0.37 ± 0.06	0.20 ± 0.01	0.24 ± 0.02	60.1	76.3	41.8	49.2
	8B	4.34	0.48 ± 0.04	0.79 ± 0.11	0.16 ± 0.01	0.26 ± 0.02	82.5	130.7	28.1	44.5
	8C	1.15	0.59 ± 0.05	1.22 ± 0.15	0.26 ± 0.02	0.35 ± 0.03	158.7	329.4	68.9	93.4
STR-9	9A	1.35	0.23 ± 0.02	0.27 ± 0.04	0.20 ± 0.01	0.21 ± 0.01	80.7	95.1	72.8	75.5
	9B	1.56	0.26 ± 0.03	0.46 ± 0.09	0.20 ± 0.01	0.23 ± 0.02	75.8	133.4	57.8	66.4

Table 6. Characteristics of cuts made in STR-5, STR-7, STR-8, and STR-9 sites.

Site		STR-5	STR-7	STR-8	STR-9
Cutting Area (ha)		44.96	18	19.86	8.09
Selective cutting grade (%)		66	33	33	50
Measured Biomass (Mg)		*1844*	*495*	*373*	*277*
Estimated Biomass (Mg ha^{-1})	Model 1	75.9	87.7	71.3	78.2
	Model 2	131.5	134.1	103.5	114.2
	Model 3	51.7	68.5	34.9	65.3
	Model 4	59.9	77.9	46.8	70.9
Total biomass (Mg)	Model 1	*2252*	*521*	*467*	*316*
	Model 2	*3902*	*797*	*678*	*462*
	Model 3	*1534*	*407*	*229*	*264*
	Model 4	*1777*	*463*	*307*	*287*

4. Discussion

The proposed methodology, thanks to the support of the new technologies, allows an accurate estimation of the wood biomass available in a riverbank environment under Consortium management, overcoming the limits of a traditional ground survey. A careful preliminary analysis of the area under investigation based on the available local orthophotos permitted five zones representative of the morpho-vegetational trees' variety to be identified. A quick pilot inspection of the riverbank segments selected for the trials was crucial to choose the accessible sites, discarding points with extremely dense vegetation, steep banks, or even closed by private-property fences.

The UAV's campaign realized over the selected riparian traits representative of the whole river network through an accurate photogrammetric reconstruction of RGB images allowed an extremely detailed orthomosaic map as well as an accurate 3D model to be acquired. The analysis of a dataset composed of both measured and remotely sensed acquired parameters allowed a system of four allometric models for estimating the trees biomass to be built (Tables 4 and 5). These models were chosen over others, which, although providing better results in terms of R^2, were found to be not fully reliable. In the case of exponential models, for example, extreme heights (that could be due to errors inside the CHM) produced an estimate exponentially out of range. Models presented in Table 4 instead show representative results (the greatest correlation is R^2 = 0.63) where such values could be a direct consequence of the high vegetation variability in terms of the species and size of trees (Section 3.1).

In this regard, given that studies on UAV biomass estimation in riparian zones are limited to [72], the results presented here are compared to these and to some scientific works within a larger scope. In particular, the comparison between UAV-predicted biomass vs. field reference biomass was considered by [58], who reported for an uneven-aged and mixed forest an R^2 value equal to 0.39 (*broadleaf species*); [82] and in a healthy subplot of *Robinia pseudoacacia* forest with UAV- LiDAR and [83] in the Mediterranean environment, R^2 reached up to 0.92 and 0.87, respectively. The current work presents higher correlation values (even for the worst model) with respect to [58] but lower ones if compared with studies that encompass regularly spaced forests with an open canopy, fairly flat terrain, and no understory [82,83]. However, if the complexity of riparian vegetation is taken as a reference point, the present study can be related to similar studies that estimate AGB in a tropical forest. As in the case of [84], which, comparing AGB obtained from UAV-RGB imagery versus AGB estimated by allometric equations starting from ground-measured H and DBH, achieved comparable R^2 (from 0.65 to 0.76). This brief comparison can give an idea of how difficult it is to estimate such a pivotal allometric parameter as biomass in a natural riparian environment.

Considering the ground-sampled parameters (Table 2), it can be noted that allometric data present relevant differences among test areas, especially for DBH and biomass. This reflects the extremely high variability in terms of the spatial distribution and multi-layer growth of spontaneous vegetation along with the watercourses. The highest values for H and DBH occurred in test area E; the possible reason why there is such tree growth could be twofold: plants could be boosted by nutrient leaching stemming from the adjacent field and/or the long time since the last management. In test area D, we can observe a specific distribution of DBH that is affected by the dense vegetation and young tree age, which influences, in turn, the low average biomass value (0.13 Mg). The lowest CD values can be found in test areas C and E (3.92 and 3.97 m, respectively) and this is probably due to a large number of black poplars and to their columnar habitus, which causes reduced crown projection.

Analyzing the UAV remotely sensed allometric parameters, i.e., H and CD, acquired for the five monitored zones, it was observed that this technology achieved good results. Indeed, comparing the measured values in test sites A–F (Table 2) with the estimated ones within the same areas (ID UAV 5A, 5B, 5D, 7A, 8A, 8C, Table 3), a good correspondence between the two datasets emerged in almost all the cases. For H, the variation ranged from −5% to +12% (with the worst result for Bruna 5A with an overestimation of +25%) while for CD, the variation was rather higher, ranging from −8% to +23% (with the worst result always for Bruna 5A with an underestimation of −57%). In particular, the lowest average height identified through ground measurements along the 5D site in the Rigo creek (10.52 m ± 2.26 m) was also highlighted through the UAV survey (10.71 m ± 3.76 m). The comparison between these two datasets allows a good validation of the remotely sensed data to be performed, although a conspicuous ground dataset was not sampled, as done in other works [27,85]. Moreover, the UAV-derived parameters are comparable with those identified with the same platform, especially for H, for example, in areas characterized by *Robinia pseudoacacia* [82] or in a pan-mixed conifer–broadleaf stand where *Acer* spp., *Salix* spp., and *Quercus crispula* are common deciduous species [58]. Instead, for CD, no references dealing with the species detected in this work were found.

Regarding tree average biomass, a high variability was observed over the sites and among the four models (Table 5). Site 5D presented very low biomass through all four models (<0.15 Mg) due to the massive presence of isolated young poplars, while the highest value (average 0.61 Mg) stemmed from 8C, where a large number of trees with considerable size were detected by the UAV flight. Besides, site 8C, together with 6D, had the highest variability among the models, which could be due to the highest number of species detected. When the site plant cover is dominated by a single tree species, as in site C and D (with 87% of poplar and 80% of *Robinia pseudoacacia*, respectively), the variability in the biomass estimation is greatly reduced. Comparing UAV-derived with ground-sampled average values (Table 2), we can see that estimations stemming from Model 3 are the closest to the in-field biomass over the sites except for 5B and 5D, which are more congruent with Model 2 and Model 1, respectively. In particular, UAV-estimated biomass for the 5B, 7A, and 8A sites differ from ground measurements by at most 0.02 Mg. Model. 2, which links only measured height (*X*-independent variable) with estimated biomass (*Y*-dependent variable), returned the highest dataset value (1.22 Mg within the 6D and 8C UAV sites) and, despite the good linkage in the 5B site, in general, it tended to overestimate the results. If Model 4 is taken as a reference (best R^2 value equal to 0.63), it is worth noting that the remotely sensed values gained a good estimation of tree average biomass. In fact, the variation range between field-measured and remotely sensed values is between −25% (5B site) and +22% (5A and 8A sites). Only site 8C (Gretano) presents a very high deviation from the in-field biomass (+74%); this could be due both to the high species variability and to the small sizes of the sampled trees within the test area with a low tree number (GDC site F, tree numbers = 19, Table 2), which in turn affected the uneven weight distribution.

Additionally, focusing on the UAV biomass per surface, it was possible to observe a wide variability in the results, and the highest wood biomass per hectare was obtained through Model 2 within parcel STR-6, along ID-UAV 6A/Asso creek and ID-UAV 6D/Ente creek (475.5 Mg/ha and 425.0 Mg/ha, respectively). This result can be attributed to the tallest tree heights found among the monitored sections (19.87 m for Asso creek and 22.44 m for Ente creek). Instead, the least amount of wood biomass obtainable from the cutting polygons was found in the 7A segment of the Rigo creek (23.0 Mg/ha) with Model 1. In this section, as also highlighted by the field surveys, lower tree heights were identified (Tables 2 and 3). This feature, in association with low vegetative cover (42% on 8.27 ha), may be the reason for the low biomass values. With the aim of comparing these results with analogous biomass per surface values obtained by UAV optical imagery, only a few studies are found in the literature for a suitable comparison in terms of species and climate conditions. In particular, [72,74,86] reported the final results in Mg of carbon per dry weight, so a 2.30 conversion factor was applied to account for the carbon/total biomass ratio [87] and wood moisture content (15%). The authors of [72] classified riparian vegetation species and estimated carbon stock for ecological purposes in a Mediterranean environment. For a plot dominated by *Acacia dealbata*, they estimated an AGB value of 442 Mg/ha, a value three times higher than the maximum for 7A (133.9 Mg/ha) dominated by a species of the same botanic family (*Robinia pseudoacacia*). The biomass gap can only be partially explained by the different species and by the different reference unit (AGB vs. dendrometric mass). The results of [86], obtained in a pan–mixed conifer–broadleaf forest also characterized by Quercus crispula, can be compared with site 5B, where the genus *Quercus* is strongly represented (50% of trees). Even in this case, our results are lower (68 vs. 189 Mg/ha). The vegetative composition and colder climate in [86] could be a possible explanation. Additionally, [74] estimated higher values (202 Mg/ha) than the poplar-dominated sites C and E in central Italy for riparian forests. In this regard, it must be noted that our study could underestimate the woody riparian biomass since it aimed to estimate dendrometric biomass, which is a fraction of AGB. The dendrometric biomass is directly linked with merchantable biomass and the choice to use it as a tree weight reference stems from the practical purpose of this study.

Considering research works that estimate biomass per surface through ground measurements, the present results are in line with literature references. The authors of [88] reported values of 76 Mg/ha in mature cork oak (*Quercus suber*) forests comparable with 55 Mg/ha of Model 4 in site 5B while an AGB of 135 Mg/ha was reported by [89]. These last values are near the ones estimated for STR-6 with Model 4. Nevertheless, the reported values for riparian biomass are highly variable in the available literature, as shown by [89] in a recent synthesis developed mostly in temperate riparian forests.

Although there are discrepancies between the UAV-estimated biomass per hectare and similar values from the literature, the results of the total harvestable biomass (Table 6) are in line with those provided by the CB6 for selective loggings. In particular, the biomass values for Model 4 (STR-5, STR-8, and STR-9) and Model 1 (STR-7) are similar to the CB6 final report with an underestimation of 4% for STR5 and STR9 and 18% for STR8, and an overestimation of 5% for STR7. The selective cutting grade is variable among the parcels, and it is dependent not only on the number of trees but also on the floodplain width, river flow, cutting frequency, and presence of roads, bridges, and buildings.

Finally, the methodology presented in this study could represent a very useful tool for public authorities because it can provide data for riparian biomass estimation in a cost-effective and timely way. In some cases, LiDAR-derived information may help to achieve high biomass accuracy estimates since it has the unique capability of measuring the three-dimensional vegetation structure, also through the extraordinary strata complexity of uneven-aged forests [15]. Although LiDAR could measure the riparian forest dendrometric features accurately, this technology is quite expensive. The authors of [90] reported a major drawback in comparison to LiDAR and photogrammetry, where the latter is limited to the characterization of the outer canopy envelope, while LiDAR can acquire the vertical profile of vegetation also operating in under-canopy conditions. Regarding the costs, [91] estimated a total cost, including field crew, of about 9300 € for UAV-LiDAR and 6800 € for UAV-SfM to measure vegetation height for 30 sites on seismic lines. Besides, UAV-RGB imagery can provide good results in estimating biomass in the complex vegetation mosaic that characterizes Mediterranean riparian systems also on a large scale (i.e., river basin area), as demonstrated by the present study. Therefore, the choice to use it could be a prototype as well as a possible solution using off-the-shelf products (UAV and RGB camera) to help public authorities in managing public resources in the context of riparian ecosystems.

5. Conclusions

The adoption of precision forestry (PF) in riparian areas is currently limited to a few studies and none of these have dealt with UAV estimation of biomass, with the exception of [72]. To fill this gap, this work aimed to identify a quick and easily reproducible UAV methodological framework for estimating biomass in riparian zones following the management activities necessary to ensure optimal hydrological safety. Future research will be oriented to (i) the development of a methodology for remote CD estimation, in order to have another parameter available to build correct models for mass estimation of basin-scale biomass; and (ii) the recognition of alien species in the Mediterranean environment that threaten biodiversity (e.g., *Robinia pseudoacacia*, *Ailanthus altissima*) using UAV-RGB technology. Additionally, it is important to optimize the accuracy and automation level of the entire workflow from data collection, image processing, and equation modeling to biomass weighing. Therefore, research can provide effective support to authorities involved in river ecosystems' management strategies in an efficient, timely, and cost-effective way. In fact, this methodology, supported by simple RGB acquisition obtained from UAV, allows its application both in different environments and at different spatial scales.

Author Contributions: A.M., P.T., V.C. and S.F.D.G. conceived the study. A.B., R.D., C.N., L.P., A.M. and S.F.D.G. performed the research and analyzed the data. A.M., A.B., V.C., R.D., C.N., L.P., P.T. and S.F.D.G. wrote the manuscript. P.T. and A.M. reviewed the draft. All authors have read and agreed to the published version of the manuscript.

Funding: This research received no external funding.

Institutional Review Board Statement: Not applicable.

Informed Consent Statement: Not applicable.

Data Availability Statement: The datasets used and analyzed during the current study are available from the corresponding author on reasonable request.

Acknowledgments: The authors wish to thank the Consorzio di Bonifica 6 Toscana Sud for taking part in the research and Regione Toscana for the river management activity.

Conflicts of Interest: The authors declare no conflict of interest.

References

1. Akasaka, T.; Akasaka, M.; Yanagawa, H. Relative importance of the environmental factors at site and landscape scales for bats along the riparian zone. *Landsc. Ecol. Eng.* **2010**, *6*, 247–255. [CrossRef]
2. Resop, J.P.; Lehmann, L.; Hession, W.C. Drone laser scanning for modeling riverscape topography and vegetation: Comparison with traditional aerial Lidar. *Drones* **2019**, *3*, 35. [CrossRef]
3. Dufour, S.; Bernez, I.; Betbeder, J.; Corgne, S.; Hubert-Moy, L.; Nabucet, J.; Rapinel, S.; Sawtschuk, J.; Trollé, C. Monitoring restored riparian vegetation: How can recent developments in remote sensing sciences help? *Knowl. Managt. Aquat. Ecosyst.* **2013**, *410*, 10. [CrossRef]
4. Van Looy, K.; Tormos, T.; Souchon, Y.; Gilvear, D. Analyzing riparian zone ecosystem services bundles to instruct river management. *Int. J. Biodivers. Sci. Ecosyst. Serv. Manag.* **2017**, *13*, 330–341. [CrossRef]
5. Camporeale, C.; Perona, P.; Ridolfi, L. Hydrological and geomorphological significance of riparian vegetation in drylands. In *Dryland Ecohydrology*; Springer: Cham, Switzerland, 2019; pp. 239–275. [CrossRef]
6. Tabacchi, E.; Lambs, L.; Guilloy, H.; Planty-Tabacchi, A.M.; Muller, E.; Decamps, H. Impacts of riparian vegetation on hydrological processes. Hydrol. *Process* **2000**, *14*, 2959–2976. [CrossRef]
7. Krzeminska, D.; Kerkhof, T.; Skaalsveen, K.; Stolte, J. Effect of riparian vegetation on stream bank stability in small agricultural catchments. *Catena* **2019**, *172*, 87–96. [CrossRef]
8. Musser, S.R.; Grafe, J.; Ortega-Achury, S.L.; Ramirez-Avila, J.J. Influence of riparian vegetation on stream health and water quality. In *World Environmental and Water Resources Congress 2019: Groundwater, Sustainability, Hydro-Climate/Climate Change, and Environmental Engineering*; American Society of Civil Engineers: Reston, VA, USA, 2019; pp. 59–67. [CrossRef]
9. Zhao, Q.; Zhang, Y.; Xu, S.; Ji, X.; Wang, S.; Ding, S. Relationships between riparian vegetation pattern and the hydraulic characteristics of upslope runoff. *Sustainability* **2019**, *11*, 2966. [CrossRef]
10. Laslier, M.; Hubert-Moy, L.; Dufour, S. Mapping riparian vegetation functions using 3D bispectral LiDAR data. *Water* **2019**, *11*, 483. [CrossRef]
11. Hupp, C.R.; Rinaldi, M. Riparian vegetation patterns in relation to fluvial landforms and channel evolution along selected rivers of Tuscany (Central Italy). *Ann. Am. Assoc. Geogr.* **2007**, *97*, 12–30. [CrossRef]
12. Michez, A.; Piégay, H.; Lejeune, P.; Claessens, H. Multi-temporal monitoring of a regional riparian buffer network (>12,000 km) with LiDAR and photogrammetric point clouds. *J. Environ. Manag.* **2017**, *202*, 424–436. [CrossRef]
13. Räpple, B.; Piégay, H.; Stella, J.C.; Mercier, D. What drives riparian vegetation encroachment in braided river channels at patch to reach scales? Insights from annual airborne surveys (Drôme River, SE France, 2005–2011). *Ecohydrology* **2017**, *10*, e1886. [CrossRef]
14. González-Jaramillo, V.; Fries, A.; Bendix, J. AGB estimation in a tropical mountain forest (TMF) by means of RGB and multispectral images using an unmanned aerial vehicle (UAV). *Remote Sens.* **2019**, *11*, 1413. [CrossRef]
15. Lefsky, M.A.; Cohen, W.B.; Harding, D.J.; Parker, G.G.; Acker, S.A.; Gower, S.T. Lidar remote sensing of above-ground biomass in three biomes. *Glob. Ecol. Biogeogr.* **2002**, *11*, 393–399. [CrossRef]
16. Lefsky, M.A.; Cohen, W.B.; Parker, G.G.; Harding, D.J. Lidar remote sensing for ecosystem studies. *Bioscience* **2002**, *52*, 19–30. [CrossRef]
17. Liang, X.; Kukko, A.; Hyyppä, J.; Lehtomäki, M.; Pyörälä, J.; Yu, X.; Kaartinen, H.; Jaakkola, A.; Wang, Y. In-situ measurements from mobile platforms: An emerging approach to address the old challenges associated with forest inventories. *ISPRS J. Photogramm. Remote Sens.* **2018**, *143*, 97–107. [CrossRef]
18. Turner, D.P.; Cohen, W.B.; Kennedy, R.E.; Fassnacht, K.S.; Briggs, J.M. Relationship between leaf area index and Landsat TM spectral vegetation indices across three temperate zone sites. *Remote Sens. Environ.* **1999**, *70*, 52–68. [CrossRef]
19. Goetz, S.J. Remote sensing of riparian buffers: Past progress and future prospects. *J. Am. Water Resour. Assoc.* **2006**, *42*, 133–143. [CrossRef]
20. Johansen, K.; Coops, N.C.; Gergel, S.E.; Stange, Y. Application of high spatial resolution satellite imagery for riparian and forest ecosystem classification. *Remote Sens. Environ.* **2007**, *110*, 29–44. [CrossRef]
21. Yang, X. Integrated use of remote sensing and geographic information systems in riparian vegetation delineation and mapping. *Int. J. Remote Sens.* **2007**, *28*, 353–370. [CrossRef]
22. Johansen, K.; Phinn, S.; Witte, C. Mapping of riparian zone attributes using discrete return LiDAR, QuickBird and SPOT-5 imagery: Assessing accuracy and costs. *Remote Sens. Environ.* **2010**, *114*, 2679–2691. [CrossRef]
23. Aguiar, F.C.; Fernandes, M.R.; Ferreira, M.T. Riparian vegetation metrics as tools for guiding ecological restoration in riverscape set. *Knowl. Managt. Aquat. Ecosyst.* **2011**, *402*, 21. [CrossRef]

24. Johansen, K.; Tiede, D.; Blaschke, T.; Arroyo, L.A.; Phinn, S. Automatic geographic object based mapping of streambed and riparian zone extent from lidar data in a temperate rural urban environment, Australia. *Remote Sens.* **2011**, *3*, 1139–1156. [CrossRef]
25. Dufour, S.; Muller, E.; Straastma, M.; Corgne, S. Image uses for riparian vegetation study and management. In *Imagery and River Management: Recent Advances and Challenging Issues*; Carbonneau, R.E., Piégay, H., Eds.; Wiley: Hoboken, NJ, USA, 2012; pp. 215–239. [CrossRef]
26. Fernandes, M.R.; Aguiar, F.C.; Ferreira, M.T.; Cardoso Pereira, J.M. Spectral separability of riparian forests from small and medium-sized rivers across a latitudinal gradient using multispectral imagery. *Int. J. Remote Sens.* **2013**, *33*, 2375–2401. [CrossRef]
27. Dalponte, M.; Reyes, F.; Kandare, K.; Gianelle, D. Delineation of individual tree crowns from ALS and hyperspectral data: A comparison among four methods. *Eur. J. Remote Sens.* **2015**, *48*, 365–382. [CrossRef]
28. Fujimoto, A.; Haga, C.; Matsui, T.; Machimura, T.; Hayashi, K.; Sugita, S.; Takagi, H. An end to end process development for uav-sfm based forest monitoring: Individual tree detection, species classification and carbon dynamics simulation. *Forests* **2019**, *10*, 680. [CrossRef]
29. Di Gennaro, S.F.; Nati, C.; Dainelli, R.; Pastonchi, L.; Berton, A.; Toscano, P.; Matese, A. An automatic UAV based segmentation approach for pruning biomass estimation in irregularly spaced chestnut orchards. *Forests* **2020**, *11*, 308. [CrossRef]
30. Navarro, A.; Young, M.; Allan, B.; Carnell, P.; Macreadie, P.; Ierodiaconou, D. The application of Unmanned Aerial Vehicles (UAVs) to estimate above-ground biomass of mangrove ecosystems. *Remote Sens. Environ.* **2020**, *242*, 111747. [CrossRef]
31. Thiel, C.; Müller, M.M.; Berger, C.; Cremer, F.; Dubois, C.; Hese, S.; Baade, J.; Pathe, C. Monitoring selective logging in a pine-dominated forest in central Germany with repeated drone flights utilizing a low cost RTK quadcopter. *Drones* **2020**, *4*, 11. [CrossRef]
32. Holopainen, M.; Vastaranta, M.; Hyyppä, J. Outlook for the next generation's precision forestry in Finland. *Forests* **2014**, *5*, 1682–1694. [CrossRef]
33. Dash, J.; Pont, D.; Brownlie, R.; Dunningham, A.; Watt, M.; Pearse, G. Remote sensing for precision forestry. *NZJ For* **2016**, *60*, 15–24.
34. Messinger, M.; Asner, G.P.; Silman, M. Rapid assessments of amazon forest structure and biomass using small unmanned aerial systems. *Remote Sens.* **2016**, *8*, 615. [CrossRef]
35. Taylor, S.; Veal, M.; Grift, T.; McDonald, T.; Corley, F. Precision Forestry: Operational Tactics for Today and Tomorrow. 25th Annual Meeting of the Council of Forest Engineers. 2002. Available online: www.eng.auburn.edu/files/file169.pdf (accessed on 3 March 2021).
36. Iglhaut, J.; Cabo, C.; Puliti, S.; Piermattei, L.; O'Connor, J.; Rosette, J. Structure from motion photogrammetry in forestry: A review. *Curr. For. Rep.* **2019**, *5*, 155–168. [CrossRef]
37. Maes, W.H.; Huete, A.R.; Avino, M.; Boer, M.M.; Dehaan, R.; Pendall, E.; Griebel, A.; Steppe, K. Can UAV-based infrared thermography be used to study plant-parasite interactions between mistletoe and Eucalypt trees? *Remote Sens.* **2018**, *10*, 2062. [CrossRef]
38. Roşca, S.; Suomalainen, J.; Bartholomeus, H.; Herold, M. Comparing terrestrial laser scanning and unmanned aerial vehicle structure from motion to assess top of canopy structure in tropical forests. *Interface Focus* **2018**, *8*, 20170038. [CrossRef] [PubMed]
39. Pádua, L.; Adão, T.; Guimarães, N.; Sousa, A.; Peres, E.; Sousa, J.J. Post-fire forestry recovery monitoring using high-resolution multispectral imagery from unmanned aerial vehicles. *Int. Arch. Photogramm. Remote Sens. Spat. Inf. Sci. ISPRS Arch.* **2019**, *42*, 301–305. [CrossRef]
40. Safonova, A.; Tabik, S.; Alcaraz-Segura, D.; Rubtsov, A.; Maglinets, Y.; Herrera, F. Detection of fir trees (*Abies sibirica*) damaged by the bark beetle in unmanned aerial vehicle images with deep learning. *Remote Sens.* **2019**, *11*, 643. [CrossRef]
41. Swinfield, T.; Lindsell, J.A.; Williams, J.V.; Harrison, R.D.; Agustiono Habibi Gemita, E.; Schönlieb, C.B.; Coomes, D.A. Accurate measurement of tropical forest canopy heights and aboveground carbon using structure from motion. *Remote Sens.* **2019**, *11*, 928. [CrossRef]
42. Otsu, K.; Pla, M.; Vayreda, J.; Brotons, L. Calibrating the Severity of forest defoliation by pine processionary moth with Landsat and UAV imagery. *Sensors* **2018**, *18*, 3278. [CrossRef]
43. Zhang, N.; Zhang, X.; Yang, G.; Zhu, C.; Huo, L.; Feng, H. Assessment of defoliation during the Dendrolimus tabulaeformis Tsai et Liu disaster outbreak using UAV-based hyperspectral images. *Remote Sens. Environ.* **2018**, *217*, 323–339. [CrossRef]
44. Cardil, A.; Otsu, K.; Pla, M.; Silva, C.A.; Brotons, L. Quantifying pine processionary moth defoliation in a pine-oak mixed forest using unmanned aerial systems and multispectral imagery. *PLoS ONE* **2019**, *14*, e0213027. [CrossRef]
45. Rossi, F.C.; Fritz, A.; Becker, G. Combining Satellite and UAV imagery to delineate forest cover and basal area after mixed-severity fires. *Sustainability* **2018**, *10*, 2227. [CrossRef]
46. Larrinaga, A.R.; Brotons, L. Greenness indices from a low-cost UAV imagery as tools for monitoring post-fire forest recovery. *Drones* **2019**, *3*, 6. [CrossRef]
47. Tuominen, S.; Balazs, A.; Honkavaara, E.; Pölönen, I.; Saari, H.; Hakala, T.; Viljanen, N. Hyperspectral UAV-imagery and photogrammetric canopy height model in estimating forest stand variables. *Silva Fenn.* **2017**, *51*, 7721. [CrossRef]
48. Franklin, S.E.; Ahmed, O.S. Deciduous tree species classification using object-based analysis and machine learning with unmanned aerial vehicle multispectral data. *Int. J. Remote Sens.* **2018**, *39*, 5236–5245. [CrossRef]
49. Komárek, J.; Klouček, T.; Prošek, J. The potential of unmanned aerial systems: A tool towards precision classification of hard-to-distinguish vegetation types? *Int. J. Appl. Earth Obs. Geoinf.* **2018**, *71*, 9–19. [CrossRef]

50. Sothe, C.; Dalponte, M.; de Almeida, C.M.; Schimalski, M.B.; Lima, C.L.; Liesenberg, V.; Miyoshi, G.T.; Tommaselli, A.M.G. Tree species classification in a highly diverse subtropical forest integrating UAV-based photogrammetric point cloud and hyperspectral data. *Remote Sens.* **2019**, *11*, 1338. [CrossRef]
51. Waite, C.E.; van der Heijden, G.M.F.; Field, R.; Boyd, D.S. A view from above: Unmanned aerial vehicles (UAVs) provide a new tool for assessing liana infestation in tropical forest canopies. *J. Appl. Ecol.* **2019**, *56*, 902–912. [CrossRef]
52. Wu, H.; Wiesner-Hanks, T.; Stewart, E.L.; DeChant, C.; Kaczmar, N.; Gore, M.A.; Nelson, R.J.; Lipson, H. Autonomous detection of plant disease symptoms directly from aerial imagery. *Plant Phenome J.* **2019**, *2*, 190006. [CrossRef]
53. Jucker, T.; Caspersen, J.; Chave, J.; Antin, C.; Barbier, N.; Bongers, F.; Dalponte, M.; van Ewijk, K.I.; Forrester, D.I.; Haeni, M.; et al. Allometric equations for integrating remote sensing imagery into forest monitoring programmes. *Glob. Chang. Biol.* **2016**, *23*, 177–190. [CrossRef]
54. Carr, J.C.; Slyder, J.B. Individual tree segmentation from a leaf-off photogrammetric point cloud. *Int. J. Remote Sens.* **2018**, *39*, 5195–5210. [CrossRef]
55. Chung, C.H.; Wang, C.H.; Hsieh, H.C.; Huang, C.Y. Comparison of forest canopy height profiles in a mountainous region of Taiwan derived from airborne lidar and unmanned aerial vehicle imagery. *GISci Remote Sens.* **2019**, *56*, 1289–1304. [CrossRef]
56. Carvajal-Ramírez, F.; Marques Da Silva, J.; Agüera-Vega, F.; Martínez-Carricondo, P.; Serrano, J.; Moral García, F.J. Evaluation of fire severity indices based on pre-and post-fire multispectral imagery sensed from UAV. *Remote Sens.* **2019**, *11*, 993. [CrossRef]
57. De Luca, G.; Silva, J.; Cerasoli, S.; Araújo, J.; Campos, J.; Di Fazio, S.; Modica, G. Object-Based land cover classification of cork oak woodlands using UAV imagery and Orfeo ToolBox. *Remote Sens.* **2019**, *11*, 1238. [CrossRef]
58. Jayathunga, S.; Owari, T.; Tsuyuki, S. Digital aerial photogrammetry for uneven-aged forest management: Assessing the potential to reconstruct canopy structure and estimate living biomass. *Remote Sens.* **2019**, *11*, 338. [CrossRef]
59. McClelland, M.P.; van Aardt, J.; Hale, D. Manned aircraft versus small unmanned aerial system—Forestry remote sensing comparison utilizing lidar and structure-from-motion for forest carbon modeling and disturbance detection. *J. Appl. Remote Sens.* **2019**, *14*, 022202. [CrossRef]
60. Park, J.Y.; Muller-Landau, H.C.; Lichstein, J.W.; Rifai, S.W.; Dandois, J.P.; Bohlman, S.A. Quantifying leaf phenology of individual trees and species in a tropical forest using unmanned aerial vehicle (UAV) images. *Remote Sens.* **2019**, *11*, 32. [CrossRef]
61. Vaglio Laurin, G.; Ding, J.; Disney, M.; Bartholomeus, H.; Herold, M.; Papale, D.; Valentini, R. Tree height in tropical forest as measured by different ground, proximal, and remote sensing instruments, and impacts on above ground biomass estimates. *Int. J. Appl. Earth Obs. Geoinf.* **2019**, *82*, 101899. [CrossRef]
62. Zhang, X.; Zhang, F.; Qi, Y.; Deng, L.; Wang, X.; Yang, S. New research methods for vegetation information extraction based on visible light remote sensing images from an unmanned aerial vehicle (UAV). *Int. J. Appl. Earth Obs. Geoinf.* **2019**, *78*, 215–226. [CrossRef]
63. Alonzo, M.; Andersen, H.E.; Morton, D.C.; Cook, B.D. Quantifying boreal forest structure and composition using UAV structure from motion. *Forests* **2018**, *9*, 119. [CrossRef]
64. Dunford, R.; Michel, K.; Gagnage, M.; Piégay, H.; Trémelo, M.L. Potential and constraints of UAV technology for the characterisation of Mediterranean riparian forest. *Int. J. Remote Sens.* **2009**, *30*, 4915–4935. [CrossRef]
65. Cierjacks, A.; Kleinschmit, B.; Babinsky, M.; Kleinschroth, F.; Markert, A.; Menzel, M.; Ziechmann, U.; Schiller, T.; Graf, M.; Lang, F. Carbon stocks of soil and vegetation on Danubian floodplain. *J. Plant Nutr. Soil Sci.* **2010**, *173*, 644–653. [CrossRef]
66. Suchenwirth, L.; Forster, M.; Cierjacks, A.; Lang, F.; Kleinschmit, B. Knowledge-based classification of remote sensing data for the estimation of below- and above-ground organic carbon stocks in riparian forests. *Wetl. Ecol. Manag.* **2012**, *20*, 151–163. [CrossRef]
67. Filipi, A.M.; Güneralp, I.; Randal, J. Hyperspectral remote sensing of aboveground biomass on a river meander bend using multivariate adaptive regression splines and stochastic gradient boosting. *Remote Sens. Lett.* **2014**, *5*, 432–441. [CrossRef]
68. Güneralp, I.; Filippi, A.M.; Randall, J. Estimation of floodplain aboveground biomass using multispectral remote sensing and nonparametric modeling. *Int. J. Appl. Earth Obs. Geoinf.* **2014**, *33*, 119–126. [CrossRef]
69. Hortobágyi, B.; Vautier, F.; Burkart, A.; Wrobel, T.J.; Peiry, J.L.; Steiger, J.; Corenblit, D.J.F. Use of photogrammetry for the study of riparian vegetation dynamics. In Proceedings of the IS Rivers-2e Conférence Internationale "Recherches et Actions au service des fleuves et grandes rivières", Lion, France, 22–26 June 2015; Available online: https://asso.graie.org/isrivers/en/isrivers-2018/isrivers-2015/ (accessed on 10 November 2021).
70. Michez, A.; Piégay, H.; Jonathan, L.; Claessens, H.; Lejeune, P. Mapping of riparian invasive species with supervised classification of Unmanned Aerial System (UAS) imagery. *Int. J. Appl. Earth Obs. Geoinf.* **2016**, *44*, 88–94. [CrossRef]
71. Michez, A.; Piégay, H.; Lisein, J.; Claessens, H.; Lejeune, P. Classification of riparian forest species and health condition using multi-temporal and hyperspatial imagery from unmanned aerial system. *Environ. Monit. Assess.* **2016**, *188*, 146. [CrossRef] [PubMed]
72. Fernandes, M.R.; Aguiar, F.C.; Martins, M.J.; Rico, N.; Ferreira, M.T.; Correia, A.C. Carbon stock estimations in a Mediterranean riparian forest: A case study combining field data and UAV imagery. *Forests* **2020**, *11*, 376. [CrossRef]
73. Huylenbroeck, L.; Laslier, M.; Dufour, S.; Georges, B.; Michez, A. Using remote sensing to characterize riparian vegetation: A review of available tools and perspectives for managers. *J. Environ. Manag.* **2020**, *267*, 110652. [CrossRef] [PubMed]
74. Cartisano, R.; Mattioli, W.; Corona, P.; Mugnozza, G.; Sabatti, M.; Ferrari, B.; Cimini, D.; Giuliarelli, D. Assessing and mapping biomass potential productivity from poplardominated riparian forests: A case study. *Biomass Bioenerg.* **2013**, *54*, 293–302. [CrossRef]

75. Castellani, C.; Scrinzi, G.; Tabacchi, G.; Tosi, V. Inventario Forestale Nazionale Italiano (IFNI): Tavole di Cubatura a Doppia Entrata/Istituto Sperimentale Per L'assestamento Forestale e per L'alpicoltura (MAP/ISAFA). 1984. Available online: https://www.collegiogeometri.bo.it/public/allegatiNews/1c923229-3632-445a-9151-6cce3414e617_fascicolo%20completo.pdf (accessed on 12 January 2021).
76. Wood Fuel Handbook. 2008. Available online: http://www.biomasstradecentre2.eu/available-literature/AEBIOM (accessed on 12 January 2021).
77. Khosravipour, A.; Skidmore, A.K.; Isenburg, M.; Wang, T.; Hussin, Y.A. Generating pit-free canopy height models from airborne lidar. *Photogramm. Eng. Remote Sens.* **2014**, *80*, 863–872. [CrossRef]
78. Silva, C.A.; Crookston, N.L.; Hudak, A.T.; Vierling, L.A. Package "rLiDAR". LiDAR Data Processing and Visualization. R package version 0.1.1. 2017. Available online: https://CRAN.R-project.org/package=rLiDAR (accessed on 15 May 2020).
79. Silva, C.A.; Hudak, A.T.; Vierling, L.A.; Loudermilk, E.L.; O'Brien, J.J.; Hiers, J.K.; Jack, S.B.; Gonzalez-Benecke, C.; Lee, H.; Falkowski, M.F.; et al. Imputation of individual longleaf pine (Pinus palustris Mill.) tree attributes from field and LiDAR data. *Can. J. Remote Sens.* **2016**, *42*, 554–573. [CrossRef]
80. Ganz, S.; Käber, Y.; Adler, P. Measuring tree height with remote sensing-a comparison of photogrammetric and LiDAR data with different field measurements. *Forests* **2019**, *10*, 694. [CrossRef]
81. Wilton, C.P.; da Silva, C.P. LAB Fit Curve Fitting Software. Nonlinear Regression and Treatment of Data Program, 7.2.50. 2011. Available online: http://labfit.net/ (accessed on 15 May 2020).
82. Lu, J.; Wang, H.; Qin, S.; Cao, L.; Pu, R.; Li, G.; Sun, J. Estimation of aboveground biomass of Robinia pseudoacacia forest in the Yellow River Delta based on UAV and Backpack LiDAR point clouds. *Int. J. Appl. Earth Obs.* **2020**, *86*, 102014. [CrossRef]
83. Guerra-Hernández, J.; González-Ferreiro, E.; Monleón, V.J.; Faias, S.P.; Tomé, M.; Díaz-Varela, R.A. Use of multi-temporal UAV-derived imagery for estimating individual tree growth in Pinus pinea stands. *Forests* **2017**, *8*, 300. [CrossRef]
84. Domingo, D.; Ørka, H.O.; Næsset, E.; Kachamba, D.; Gobakken, T. Effects of UAV image resolution, camera type, and image overlap on accuracy of biomass predictions in a tropical woodland. *Remote Sens.* **2019**, *11*, 948. [CrossRef]
85. Malek, S.; Miglietta, F.; Gobakken, T.; Næsset, E.; Gianelle, D.; Dalponte, M. Prediction of stem diameter and biomass at individual tree crown level with advanced machine learning techniques. *iForest-Biogeosci. For.* **2019**, *12*, 323–329. [CrossRef]
86. Jayathunga, S.; Owari, T.; Tsuyuki, S. The use of fixed–wing UAV photogrammetry with LiDAR DTM to estimate merchantable volume and carbon stock in living biomass over a mixed conifer–broadleaf forest. *Int. J. Appl. Earth Obs. Geoinf.* **2018**, *73*, 767–777. [CrossRef]
87. Smith, J.E.; Heath, L.S.; Hoover, C.M. Carbon factors and models for forest carbon estimates for the 2005–2011 National Greenhouse Gas Inventories of the United States. *For. Ecol. Manag.* **2013**, *307*, 7–19. [CrossRef]
88. Correia, A.C.; Tomé, M.; Pacheco, C.A.; Faias, S.; Dias, A.C.; Freire, J.; Carvalho, P.O.; Pereira, J.S. Biomass allometry and carbon factors for a Mediterranean pine (*Pinus pinea* L.) in Portugal. *For. Syst.* **2010**, *19*, 418–433. [CrossRef]
89. Dybala, K.E.; Matzek, V.; Gardali, T.; Seavy, N.E. Carbon sequestration in riparian forests: A global synthesis and meta-analysis. *Glob. Chang. Biol.* **2019**, *25*, 57–67. [CrossRef]
90. Dainelli, R.; Toscano, P.; Di Gennaro, S.F.; Matese, A. Recent advances in Unmanned Aerial Vehicles forest remote sensing—A systematic review. Part II: Research applications. *Forests* **2021**, *12*, 397. [CrossRef]
91. Chen, S.; McDermid, G.; Castilla, G.; Linke, J. Measuring vegetation height in linear disturbances in the boreal forest with UAV photogrammetry. *Remote Sens.* **2017**, *9*, 1257. [CrossRef]